Article

Effective terahertz shielding properties of extreme graphene-silver nanowire surfaces investigated by nanoprobing

Nano-slot chip → AgNWs spray → GO spray → GO reduction

Geon Lee, Sung Jun Kim, Yeeun Roh, Sang-Hun Lee, Dai-Sik Kim, Sang Woo Kim, Minah Seo

swkim@kist.re.kr (S.W.K.)
mseo@kist.re.kr (M.S.)

Highlights

THz shielding is performed by hybridized metamaterials with silver nanowires and rGO

Reliable monitoring tool for understanding of electromagnetic wave shielding mechanism

Article

Effective terahertz shielding properties of extreme graphene-silver nanowire surfaces investigated by nanoprobing

Geon Lee,[1,2,8] Sung Jun Kim,[3,8] Yeeun Roh,[1,4] Sang-Hun Lee,[5] Dai-Sik Kim,[2,6] Sang Woo Kim,[3,*] and Minah Seo[1,7,9,*]

SUMMARY

In the terahertz (THz) electromagnetic wave regime, which has recently received great attention in the fields of communication and security, shielding of THz waves is a significant issue. Therefore, carbon-based nanostructures or polymer–carbon nanocomposites have been widely explored. Herein, significantly enhanced THz shielding efficiency is reported for silver nanowires coated with reduced graphene oxide (rGO) and nanoscale THz metamaterials, as compared to the cases without nanoscale metamaterials. Using a nanoslot-patterned metamaterial with strong resonances at certain frequencies, THz transmission in intensity is enhanced up to three orders of magnitude. Enhanced transmission by nanopatterns substantially increases the shielding performance to the external THz waves, even for ultrathin films (several tens of nanometers) produced by a simple spray of rGO (a few nm of flakes) on a complex random nanowire network. Excellent shielding performance is presented and the shielding mechanism is investigated by the nanoprobing configuration at the same time.

INTRODUCTION

The THz-integrated technology has emerged as a promising technology for various applications, such as wireless communication (Yang et al., 2020b), nondestructive detection (Kato et al., 2016), biomedical sensing (Lee et al., 2020a; 2020b), imaging (Stantchev et al., 2020), spectroscopy (Choi et al., 2019b), and security (Federici et al., 2005; Gui et al., 2019). Recently, the THz band has gained attention as a nondestructive security system and intrachip/interchip communication as a high-speed connection, because it is harmless and uses non-ionizing radiation (Aqlan et al., 2021; Liang et al., 2015). In particular, sub-THz frequencies (100 GHz–1 THz) constitute the next-generation wireless communication network band according to the rapid growth of Internet technology and demands of broad bandwidth and ultrahigh data rates, up to terabits per second, over long distances (Rappaport et al., 2019; Zhang et al., 2019). As applications become more diverse and the development of photonic or electronic devices for efficient generation, dynamic detection, and active control increases, "shielding" becomes an important keyword, especially in terms of protecting a waveguide from unwanted interference from external electromagnetic sources. Various types of composite films with conductive material flakes, including carbon nanotubes (Park et al., 2015), graphene (Zdrojek et al., 2018), MXenes (Lin et al., 2020), and metal nanowires (Kim et al., 2013), have been introduced for high-efficiency THz electromagnetic interference (EMI) shielding.

A random network of metal nanowires is a promising candidate for outstanding shielding material owing to its high conductivity, easy fabrication, thinness (a few tens of nanometers), flexibility, and compatibility with curved surfaces. Among them, silver nanowire networks can be conveniently made with excellent electrical properties through spraying or spin coating methods. These unique characteristics enable silver nanowires to substitute bulk silver films, maintaining the merit of the nanostructure with high surface-to-volume ratio. Moreover, additional methods can further increase shielding efficiency (SE), including high-temperature sintering (Choi et al., 2019a; Gu et al., 2020), mechanical pressing (Li et al., 2021; Yang et al., 2021), light-induced welding (Kim et al., 2021), and composites with other materials (Chen et al., 2020; Hu et al., 2012; Jia et al., 2021; Wan et al., 2018; Zhou et al., 2020). However, their mechanism for preventing signal interference is not yet fully understood owing to the huge scale mismatch between the relatively long wavelength (micrometer to centimeter) and the flake size (mostly nanoscale). The absence of probing techniques to directly observe the change in optical/electrical properties at the long-wavelength regime and

[1]Sensor System Research Center, Korea Institute of Science and Technology (KIST), Seoul 02792, Republic of Korea

[2]Department of Physics and Astronomy, Seoul National University, Seoul 08826, Republic of Korea

[3]Clean Energy Research Center, Korea Institute of Science and Technology (KIST), Seoul 02792, Republic of Korea

[4]Display and Nano System Laboratory, School of Electrical Engineering, Korea University, Seoul 02841, Republic of Korea

[5]Department of Optical Engineering, Kumoh National Institute of Technology, Gumi, Gyeongbuk 39177, Republic of Korea

[6]Department of Physics and Quantum Photonics Institute, Ulsan National Institute of Science and Technology (UNIST), Ulsan 44919, Republic of Korea

[7]KU-KIST Graduate School of Converging Science and Technology, Korea University, Seoul 02841, Republic of Korea

[8]These authors contributed equally

[9]Lead contact

*Correspondence: swkim@kist.re.kr (S.W.K.), mseo@kist.re.kr (M.S.)

https://doi.org/10.1016/j.isci.2022.104033
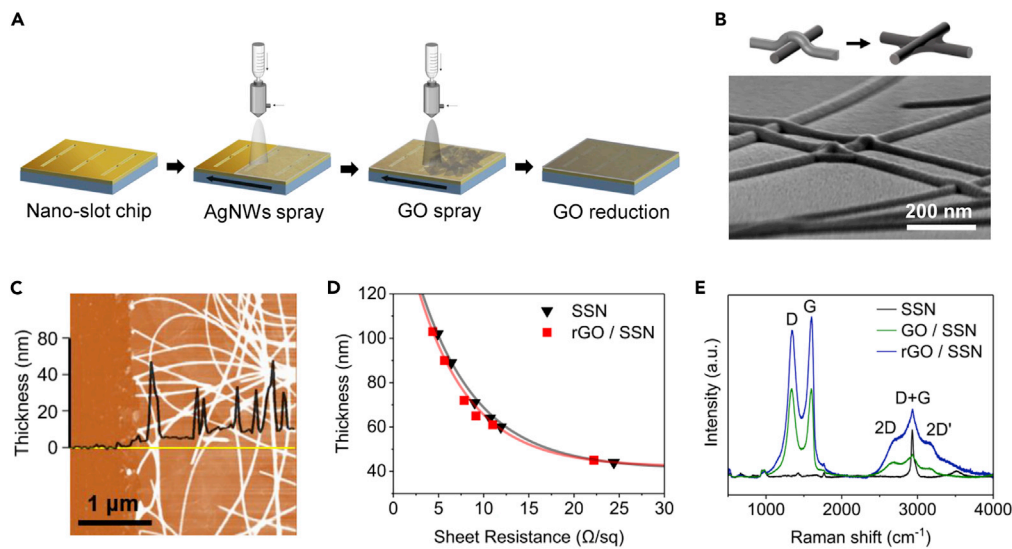
Figure 1. rGO/SSN film fabrication and measured characteristics

(A) Schematic of the fabrication process of SSN with the rGO film on Au nanoslot chips.

(B) Scanning electron microscope (SEM) image of silver nanowires with the rGO film structure (Scale bar, 200 nm). Inset scheme shows the linking process after sintering.

(C) Atomic force microscope (AFM) image for the surface profile of an rGO/SSN film; the black line denotes thickness (Scale bar, 1 μm).

(D) Measured film thickness according to the sheet resistance.

(E) Raman spectra of an SSN film, GO/SSN film, and rGO/SSN film.

occurring on the extreme surface of the thin films or network nanostructures, where the electromagnetic waves are effectively blocked, has slowed fundamental study.

Herein, we present a substantially enhanced THz wave SE using a sintered silver nanowire (SSN) network and coated reduced graphene oxide (rGO) film on a nanoslot array. A dynamic ability is demonstrated for future applications with easy film fabrication through a simple spray method. A solution containing silver nanowires and graphene oxide flakes were dropcasted onto a nanoslot array, forming an ultrathin film that was subsequently utilized for THz measurements. The rGO-treated nanoslot array shows a great decrease in the THz transmission, signifying shielding enhancement of the incident THz wave. This improved SE is caused by a strongly localized THz field originating from the enhanced absorption of the film. Furthermore, the nanoslot accompanying the strong THz field confinement can help investigate the extreme surface of the film, elucidating the shielding mechanism. The developed THz nanoprobing system via nanoslot array can be applied toward direct and nondestructive detection of extreme surface properties of film-type materials.

RESULTS AND DISCUSSION

Ultrafast surface dynamics and various optical properties of film-type materials have been examined by the THz nano-metamaterials in a non-contact manner in earlier research (Choi et al., 2018). Taking advantage of the confined THz near-field and adjustable volume at the nanoscale, surface properties have been effectively measured, even for bulk semiconductors (Si, InP, and GaAs) (Choi et al., 2017). Such "nanoprobing" using nano-patterned metal can be applied to investigate the shielding mechanism for extremely thin films, for example, graphene (Lee et al., 2020a; Lim et al., 2018). The huge difference in scale between the thickness (almost a monolayer to a few tens of nanometers) and the relatively longer wavelength (micrometer scale) is too large to intuitively and directly understand the shielding mechanism. With clever ways of decreasing the scope size, the behavior of electromagnetic waves at such local areas can be studied fundamentally and ultimately shows great potential for commercial application.

For efficient nanoprobing, a nanoslot was fabricated by conventional photolithography (Figure 1A, see STAR Methods). Figure 1B shows a field-emission scanning electron microscopy (Nova SEM; FEI) image of the rGO/SSN coated on a PET substrate.

Table 1. Measured thickness and sheet resistance depending on the number of SSN coating cycles

sample[a]	# of coating cycles	thickness (nm)	sheet resistance (Ω/sq)	sample[b]	# of coating cycles	thickness (nm)	sheet resistance (Ω/sq)
S1	4	44	24.4	R1	4	45	22.2
S2	6	60	11.9	R2	6	61	11
S3	8	64	10.7	R3	8	65	9.14
S4	10	71	9	R4	10	72	7.84
S5	14	89	6.4	R5	14	90	5.66
S6	17	102	4.9	R6	17	103	4.36

[a]Samples indicated by an S represent SSN films without the rGO coating.
[b]Samples indicated by an R represent SSN films with the rGO coating.

Atomic force microscopy (AFM) was employed to measure thicknesses of the SSN and the rGO/SSN film (Figure 1C), providing the thickness of each nanowire. The SSN films were coated using six different cycles and each SSN film was treated with and without an rGO film. The effective thickness for the SSN and rGO/SSN films was defined as the mean value of thicknesses on all surface areas. The effective thickness increases monotonically in accordance with the coating cycles in both the SSN and rGO/SSN films. More details of this value are provided in Table 1. The sheet resistances of the films were measured using a four-point probe measurement. The relation between sheet resistance and effective film thickness is plotted in Figure 1D, which shows that sheet resistance is inversely proportional to the coating cycle. For every thickness, the sheet resistance of the rGO/SSN film is slightly less than the SSN film without rGO. The SSN with GO and rGO films was also evaluated with Raman spectroscopy to verify proper formation of the rGO film (Figure 1E). The characteristic peak ratio, $I(D)/I(G)$, which is proportional to oxide defects in graphene, shows that GO was effectively reduced to rGO owing to the chemical reduction process (Díez-Betriu et al., 2013).

THz transmittance of sample using a THz time-domain spectroscopy (TDS) system is demonstrated in Figure 2 (see STAR Methods). The measured THz transmission for a nanoslot with the SSN film shows a decreased behavior compared with a nanoslot without a SSN film (inset of Figure 2A). It is noted that the discrepancy in scale between the wavelength and diameter of the nanowire is over 50,000; therefore, it is impossible to observe them without any additional signal enhancer owing to the diffraction limit (Figure 2B).

The THz transmittance was measured for SSN films coated with various coating cycles onto a bare PET film (Figure 2C) and a nanoslot chip (Figure 2D). The transmission is inversely proportional to the coating cycle for both SSN films and decreased by three orders of magnitude after 17 cycles, implying much better shielding performance compared with other nanowires introduced in earlier works (van Hoof et al., 2020). Moreover, further improved shielding ability was observed for both cases after rGO was sprayed onto the films. The rGO coating, even on the PET film, slightly reduces transmittance in Figure 2C, but note that this reduction is not so significant. In stark contrast to the PET substrate, the nanoslot cases represent noticeable changes with a decaying trend when coated with rGO, implying an increase in SE at the fundamental resonance frequency (0.65 THz). It is noted that rGO plays a role in increasing conductivity, especially for the more tightly connected SSN network on the nanoslot, but not significantly on the PET. Owing to the large dimension mismatch between the THz wavelength and nanowire size, the nanowire network on the PET substrate can be effectively considered a thin film. Then, the SE is dominantly affected only by the filling factor of the silver nanowire, regardless of nanowire linking. In this situation, the enhanced electrical connection between nanowires through the addition of thin rGO is not responsible for THz shielding. In the nanoslot, on the other hand, the THz field is extremely localized in a few hundred-nanometer-scaled slots and is able to enhance the absorption cross section (Park et al., 2013) of the nanowires. Thus, the enhanced THz field in the nanoslot can probe the charge dynamics in the network of individual nanowires, contributing to an enlarged THz SE. Nanowires, intertwined and connected on the nanoslot, form electrical circuits with multi-point connections that are sensitive to contact resistance. This resistance between nearest nanowires can be effectively reduced by the welding effect of the rGO coating. It is emphasized that the developed nanoprobing system can directly investigate these electrical linking effects
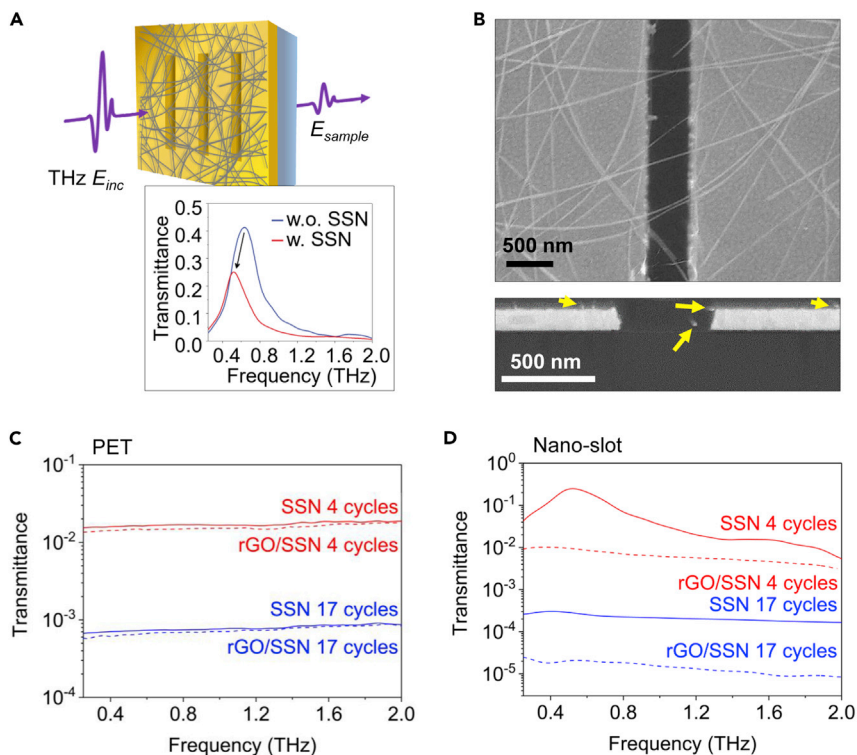
Figure 2. Far-field THz-TDS transmission measurement

(A) Schematic description of the THz transmission measurement through the SSN film. Inset presents the normalized transmittance for chips with/without an SSN film.

(B) Top and cross-view SEM images of SSNs on a nanoslot (Scale bar, 500 nm). Yellow arrows indicate each single silver nanowire. (C and D) THz transmittance for different spray coating cycles of the SSN and existence of the rGO coating on a (C) PET substrate and (D) nanoslot chip.

between nanowire networks at extremely local areas, providing an explicit interpretation for the shielding mechanism when using nanowires.

For deeper understanding, the THz spectrum was calculated by finite element method (FEM) simulation using COMSOL Multiphysics. Figure 3 demonstrates simulation results that prove the effect of the nanoslot with respect to energy consumption. The insets of Figures 3A and 3B show schematics of a THz wave through a single silver nanowire on a bare silicon substrate and nanoslot, respectively. For direct comparison of these two cases, the calculated power ($\overrightarrow{P}$) is normalized by the maximum value of the nanowire on a bare substrate ($\overrightarrow{P_0}$). In Figure 3A, THz energy consumption is rarely observed in the nanowire owing to dimension mismatch. By adapting a nanoslot, however, charges in the nanowire can overcome the dimension differences and absorb incident waves. Figure 3B shows the enhanced THz absorption from charge in the nanowire with a nanoslot at resonance frequency.

To gain further insight into the THz shielding phenomena of the hybridized SSN complex, the nanoslot, and the rGO and to explore the role of each component, THz shielding was analyzed in terms of the spray cycle. The EMI SE results were extracted from the THz transmission measurement (Figure 4). SE of the SSN and rGO/SSN film is calculated by the following equation:

$$SE = -10 \log\left(\frac{T_{sample}}{T_{subs}}\right),$$

where T_{sample} is the THz transmittance of the SSN or rGO/SSN film on the substrate platform, and T_{subs} is the transmittance of the bare substrate platform. Figures 4A and 4B illustrate the SE spectra of the SSN and rGO/SSN films on a PET substrate, meanwhile Figures 4C and 4D show the SE spectra of the SSN and rGO/SSN films on a nanoslot in the 0.25–2.0 THz range, in order to extract the effect of the film only. In Figures 4A
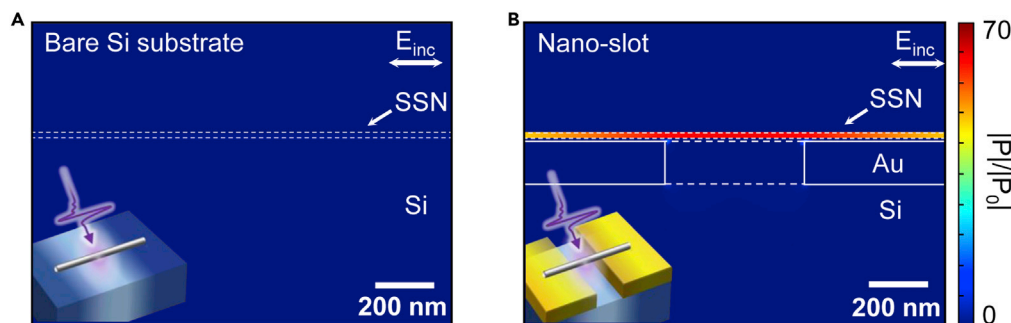
Figure 3. Distributions of power loss $(\vec{P})$ of silver nanowire
(A and B) Calculated THz losses on a (A) bare Si substrate and (B) nanoslot with single silver nanowires at resonance frequency (Scale bar, 200 nm).

and 4B, the SE of the SSN film is monotonically increased with the coating cycle. The SE is increased for coating cycles from four to six, owing to charge percolation (Hong et al., 2017), and is slightly saturated with more coatings. The native property of silver in the THz region causes gradual decrease in SE for all cases when the frequency increases.

On the contrary, as shown in Figures 4C and 4D, a different trend is observed for the SSN film on a nanoslot. The characteristic resonance at 0.65 THz is shown, which indicates the maximum SE via the nanoslot acting as a THz resonator. At the early coating cycles (~4–8 coatings), both SSN and rGO/SSN films on the nanoslot show lower SE than those on bare PET, but the SE values on the nanoslots rapidly increase as the cycle repeats.

In particular, the rGO acts as a SE enhancer, which increases SE by approximately 10 dB for the SSN film on the nanoslot. Such SE enhancement can be attained at any requisite frequency by simply tuning the geometry of the nanoslot design (Kang et al., 2018). This unrestricted modulation of working frequency (wavelength) range enables various applications that need partial shielding at the intended frequency, such as a filter.

Figure 5 summarizes the SE of THz electromagnetic waves in terms of sheet resistance at the resonance frequency of the nanoslot ($f_{res.}$ = 0.65 THz). For the SSN film on a PET substrate shown in Figure 5A, tiny SE differences occur with rGO addition. In stark contrast, the SSN film on nanoslot chips shown in Figure 5B indicates great improvement of SE with rGO addition, >10 dB. The SE property trend in terms of SSN concentration follows the model for bulk sheet resistance (Sorel et al., 2012). The SSN film on the PET substrate can be considered an effective thin film, irrespective of rGO addition (Figure 5A). Thus, the percolation between wires does not contribute to the SE owing to the huge mismatch between wavelength and nanowire dimension. Meanwhile, on the nanoslot, the SSN film induces a rapid change of the SE due to increase of sheet resistance. Because the localized field at the nanometer scale is matched to the dimension of the wire, each wire and wire network sensitively affect transmittance change. Owing to the sensitivity to the nanoscopic structure related to charge transport, rGO can enhance the interwire charge percolation that leads to remarkable SE enhancement. To demonstrate the enhanced shielding property using a nanoslot, the SEs of all cases are summarized in Figure 5C according to the SE of the PET substrate. As a criterion to evaluate the SE, an equivalent SE line is plotted as a dashed line that indicates the same SE for PET substrates and nanoslots. The enhanced SE values obtained using the nanoslot are observed above the equivalent SE line, which means higher SE, whereas lower SE is presented below the line. For lower SE cases, the absence of rGO on a nanoslot restricts charge percolation and limits SE enhancement. SE values of SSN and rGO/SSN films are proportional to coating cycles. Notably, the slope is steeper for these values compared to the equivalent SE, which implies rapid change of the SE by use of a nanoslot. The results show that a highly increased THz shielding property of a silver nanowire network is achieved with improved charge percolation owing to rGO coating and THz absorption via the nanoslot structure.

Conclusion

In conclusion, we performed the THz-TDS measurement to characterize the optical and electrical properties of SSN films with and without the rGO coating. The rGO coating significantly enhanced the shielding properties in the reliable THz frequency regime when hybridized with nanoslot arrays. The combination of an rGO-coated SSN network and nanoslot with a thickness of a few tens of nanometers can enhance
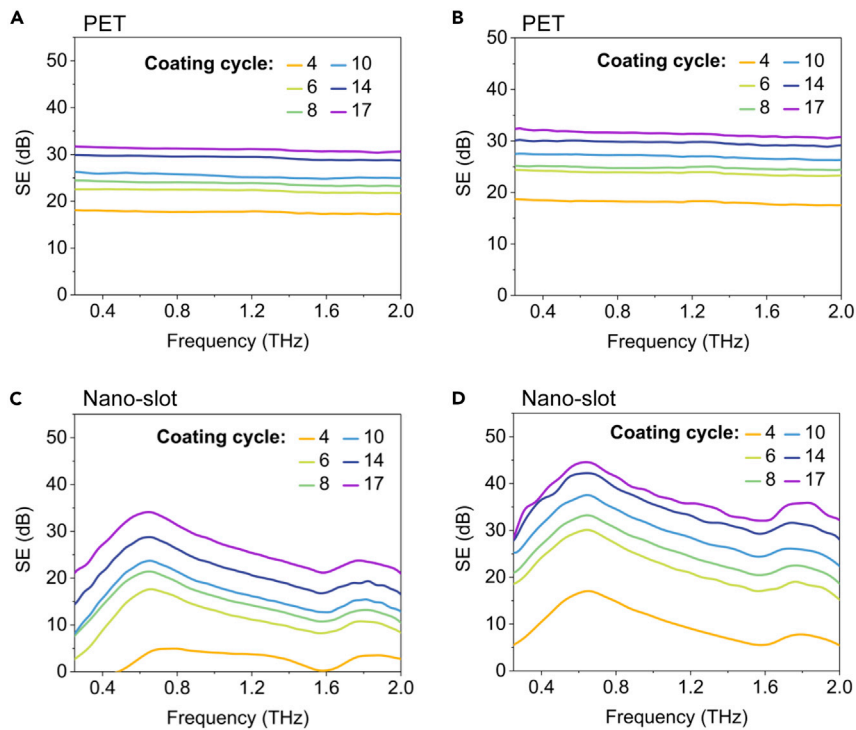
Figure 4. EMI SE of silver nanowire networks in THz regime

(A–D) (A) SSN film and (B) SSN with the rGO film on PET substrates, and (C) SSN film and (D) SSN with the rGO film on nanoslot chips.

transmission shut-off by four orders of magnitude, allowing active use of nanoscale thin films for controlling the THz-frequency electromagnetic waves. Moreover, this phenomenon was interpreted using the inter-nanowire charge percolation theory. As THz waves are further investigated for use in next-generation wireless networks, the type of shielding device suggested herein, which can be easily produced in a large area and can be target frequency-controlled freely, will be of interest to a broad community. Furthermore, by decreasing nanoslot sizes to the nanoscale to investigate extreme near-surfaces only, we have taken a step closer to understand the shielding mechanism.

Limitations of the study

The shielding performance of silver nanowires sprayed onto the nanoslot system is significantly sensitive with interwire percolation. However, various techniques that can enhance charge percolation, such as
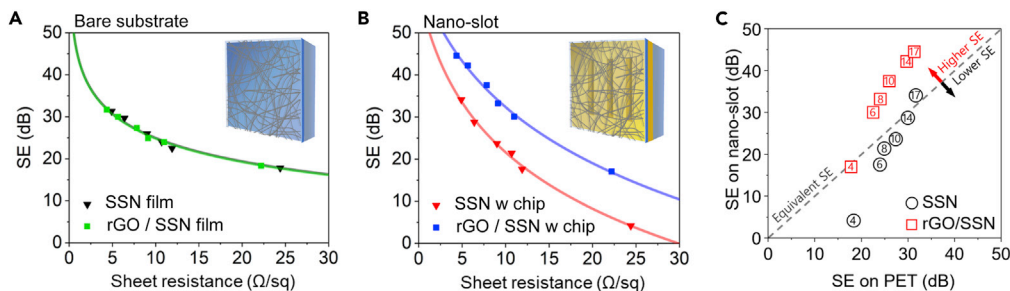
Figure 5. EMI SE in the specific THz frequency range

(A and B) (A) SSN and rGO/SSN films on PET substrates and (B) SSN and rGO/SSN films on nanoslot chips. The trends of each film type are presented by solid lines in (A) and (B).

(C) Equivalent SE comparison between SSN and rGO/SSN films on both PET and nanoslot substrates. The numbers in the symbols indicate the number of coating cycles.

mechanical pressing, chemical treatment, and laser welding, are limited because they cause deformation of gold nanoslots. Therefore, other compatible materials or nanostructures must be further investigated.

STAR★METHODS

Detailed methods are provided in the online version of this paper and include the following:

- KEY RESOURCES TABLE
- RESOURCE AVAILABILITY
  - Lead contact
  - Materials availability
  - Data and code availability
- EXPERIMENTAL MODEL AND SUBJECT DETAILS
- METHOD DETAILS
  - Sample preparation
  - THz time-domain spectroscopy
- QUANTIFICATION AND STATISTICAL ANALYSIS

AUTHOR CONTRIBUTIONS

Conceptualization, G.L. and M.S.; methodology, G.L. and S.H.L.; software, G.L. and Y.R.; formal analysis, G.L., Y.R., S.H.L., and M.S.; investigation, G.L.; resources, S.J.K. and S.W.K.; writing-original draft, G.L., Y.R., S.H.L., and M.S.; supervision, D.S.K., S.W.K., and M.S.; funding acquisition, D.S.K. and M.S.

DECLARATION OF INTERESTS

The authors declare no competing interests.

REFERENCES

Aqlan, B., Himdi, M., Vettikalladi, H., and Le-Coq, L. (2021). A 300-GHz low-cost high-gain fully metallic Fabry–Perot cavity antenna for 6G terahertz wireless communications. Sci. Rep. *11*, 1–9. https://doi.org/10.1038/s41598-021-87076-3.

Chen, W., Liu, L.X., Zhang, H.B., and Yu, Z.Z. (2020). Flexible, transparent, and conductive Ti3C2TxMXene-silver nanowire films with smart acoustic sensitivity for high-performance electromagnetic interference shielding. ACS Nano *14*, 16643–16653. https://doi.org/10.1021/acsnano.0c01635.

Choi, G., Bahk, Y.M., Kang, T., Lee, Y., Son, B.H., Ahn, Y.H., Seo, M., and Kim, D.S. (2017). Terahertz nanoprobing of semiconductor surface dynamics. Nano Lett. *17*, 6397–6401. https://doi.org/10.1021/acs.nanolett.7b03289.

Choi, G., Shahzad, F., Bahk, Y.M., Jhon, Y.M., Park, H., Alhabeb, M., Anasori, B., Kim, D.S., Koo, C.M., Gogotsi, Y., et al. (2018). Enhanced terahertz shielding of MXenes with nano-metamaterials. Adv. Opt. Mater. *6*, 1–6. https://doi.org/10.1002/adom.201701076.

Choi, J.H., Lee, K.Y., and Kim, S.W. (2019a). Ultra-bendable and durable Graphene–Urethane composite/silver nanowire film for flexible transparent electrodes and electromagnetic-interference shielding. Compos. B Eng. *177*, 107406. https://doi.org/10.1016/j.compositesb.2019.107406.

Choi, W.J., Cheng, G., Huang, Z., Zhang, S., Norris, T.B., and Kotov, N.A. (2019b). Terahertz circular dichroism spectroscopy of biomaterials enabled by kirigami polarization modulators. Nat. Mater. *18*, 820–826. https://doi.org/10.1038/s41563-019-0404-6.

Díez-Betriu, X., Álvarez-García, S., Botas, C., Álvarez, P., Sánchez-Marcos, J., Prieto, C., Menéndez, R., and De Andrés, A. (2013). Raman spectroscopy for the study of reduction mechanisms and optimization of conductivity in graphene oxide thin films. J. Mater. Chem. C *1*, 6905–6912. https://doi.org/10.1039/c3tc31124d.

Federici, J.F., Schulkin, B., Huang, F., Gary, D., Barat, R., Oliveira, F., and Zimdars, D. (2005). THz imaging and sensing for security applications - explosives, weapons and drugs. Semicond. Sci. Technol. *20*, S266–S280. https://doi.org/10.1088/0268-1242/20/7/018.

Gu, J., Hu, S., Ji, H., Feng, H., Zhao, W., Wei, J., and Li, M. (2020). Multi-layer silver nanowire/polyethylene terephthalate mesh structure for highly efficient transparent electromagnetic interference shielding. Nanotechnology *31*, 185303. https://doi.org/10.1088/1361-6528/ab6d9d.

Gui, S., Li, J., and Pi, Y. (2019). Security imaging for multi-target screening based on adaptive scene segmentation with terahertz radar. IEEE Sens. J. *19*, 2675–2684. https://doi.org/10.1109/JSEN.2018.2889884.

Hong, J.T., Park, S.J., Park, J., Lee, S., and Ahn, Y.H. (2017). Terahertz slot antenna devices fabricated on silver nanowire network films. Opt. Mater. Express 7, 1679. https://doi.org/10.1364/ome.7.001679.

Hu, M., Gao, J., Dong, Y., Li, K., Shan, G., Yang, S., and Li, R.K.Y. (2012). Flexible transparent PES/silver nanowires/PET sandwich-structured film for high-efficiency electromagnetic interference shielding. Langmuir *28*, 7101–7106. https://doi.org/10.1021/la300720y.

Jia, H., Yang, X., Kong, Q.Q., Xie, L.J., Guo, Q.G., Song, G., Liang, L.L., Chen, J.P., Li, Y., and Chen, C.M. (2021). Free-standing, anti-corrosion, super flexible graphene oxide/silver nanowire thin films for ultra-wideband electromagnetic interference shielding. J. Mater. Chem. A *9*, 1180–1191. https://doi.org/10.1039/d0ta09246k.

Kang, J.H., Kim, D.S., and Seo, M. (2018). Terahertz wave interaction with metallic nanostructures. Nanophotonics 7, 763–793. https://doi.org/10.1515/nanoph-2017-0093.

Kato, M., Tripathi, S.R., Murate, K., Imayama, K., and Kawase, K. (2016). Non-destructive drug inspection in covering materials using a terahertz spectral imaging system with injection-seeded terahertz parametric generation and detection. Opt. Express *24*, 6425. https://doi.org/10.1364/oe.24.006425.

Kim, J., Maeng, I., Jung, J., Song, H., Son, J.H., Kim, K., Lee, J., Kim, C.H., Chae, G., Jun, M., et al. (2013). Terahertz time-domain measurement of non-Drude conductivity in silver nanowire thin films for transparent electrode applications. Appl. Phys. Lett. *102*, 011109. https://doi.org/10.1063/1.4773179.

Kim, D.G., Choi, J.H., Choi, D.K., and Kim, S.W. (2018). Highly bendable and durable transparent electromagnetic interference shielding film prepared by wet sintering of silver nanowires. ACS Appl. Mater. Inter. *10*, 29730–29740. https://doi.org/10.1021/acsami.8b07054.

Kim, S.J., Yoon, H.G., and Kim, S.W. (2021). Extremely robust and reliable transparent silver nanowire-mesh electrode with multifunctional optoelectronic performance through selective laser nanowelding for flexible smart devices. Adv. Eng. Mater. *23*, 1–11. https://doi.org/10.1002/adem.202001310.

Lee, S.H., Lee, D., Choi, M.H., Son, J.H., and Seo, M. (2019). Highly sensitive and selective detection of steroid hormones using terahertz molecule-specific sensors. Anal. Chem. *91*, 6844–6849. https://doi.org/10.1021/acs.analchem.9b01066.

Lee, S.H., Choe, J.H., Kim, C., Bae, S., Kim, J.S., Park, Q.H., and Seo, M. (2020a). Graphene assisted terahertz metamaterials for sensitive bio-sensing. Sens. Actuator. B *310*, 127841. https://doi.org/10.1016/j.snb.2020.127841.

Lee, S.H., Shin, S., Roh, Y., Oh, S.J., Lee, S.H., Song, H.S., Ryu, Y.S., Kim, Y.K., and Seo, M. (2020b). Label-free brain tissue imaging using large-area terahertz metamaterials. Biosens. Bioelectron. *170*, 112663. https://doi.org/10.1016/j.bios.2020.112663.

Li, S., Qian, K., Thaiboonrod, S., Wu, H., Cao, S., Miao, M., Shi, L., and Feng, X. (2021). Flexible multilayered aramid nanofiber/silver nanowire films with outstanding thermal durability for electromagnetic interference shielding. Compos. Appl. Sci. Manuf. *151*, 106643. https://doi.org/10.1016/j.compositesa.2021.106643.

Liang, Y., Yu, H., Zhang, H.C., Yang, C., and Cui, T.J. (2015). On-chip sub-terahertz surface plasmon polariton transmission lines in CMOS. Sci. Rep. *5*, 1–13. https://doi.org/10.1038/srep14853.

Lim, C., Lee, S.H., Jung, Y., Son, J.H., Choe, J.H., Kim, Y.J., Choi, J., Bae, S., Kim, J.H., Blick, R., et al. (2018). Broadband characterization of charge carrier transfer of hybrid graphene-deoxyribonucleic acid junctions. Carbon *130*, 525–531. https://doi.org/10.1016/j.carbon.2018.01.049.

Lin, Z., Liu, J., Peng, W., Zhu, Y., Zhao, Y., Jiang, K., Peng, M., and Tan, Y. (2020). Highly stable 3D Ti3C2Tx MXene-based foam architectures toward high-performance terahertz radiation shielding. ACS Nano *14*, 2109–2117. https://doi.org/10.1021/acsnano.9b08832.

Park, H.R., Ahn, K.J., Han, S., Bahk, Y.M., Park, N., and Kim, D.S. (2013). Colossal absorption of molecules inside single terahertz nanoantennas. Nano Lett. *13*, 1782–1786. https://doi.org/10.1021/nl400374z.

Park, H.R., Namgung, S., Chen, X., and Oh, S.H. (2015). High-density metallic nanogap arrays for the sensitive detection of single-walled carbon nanotube thin films. Faraday Discuss *178*, 195–201. https://doi.org/10.1039/c4fd00233d.

Rappaport, T.S., Xing, Y., Kanhere, O., Ju, S., Madanayake, A., Mandal, S., Alkhateeb, A., and Trichopoulos, G.C. (2019). Wireless communications and applications above 100 GHz: opportunities and challenges for 6G and beyond. IEEE Access 7, 78729–78757. https://doi.org/10.1109/ACCESS.2019.2921522.

Sorel, S., Lyons, P.E., De, S., Dickerson, J.C., and Coleman, J.N. (2012). The dependence of the optoelectrical properties of silver nanowire networks on nanowire length and diameter. Nanotechnology *23*, 185201. https://doi.org/10.1088/0957-4484/23/18/185201.

Stantchev, R.I., Yu, X., Blu, T., and Pickwell-MacPherson, E. (2020). Real-time terahertz imaging with a single-pixel detector. Nat. Commun. *11*, 1–8. https://doi.org/10.1038/s41467-020-16370-x.

van Hoof, N., Parente, M., Baldi, A., and Rivas, J.G. (2020). Terahertz time-domain spectroscopy and near-field microscopy of transparent silver nanowire networks. Adv. Opt. Mater. *8*, 1–7. https://doi.org/10.1002/adom.201900790.

Wan, Y.J., Zhu, P.L., Yu, S.H., Sun, R., Wong, C.P., and Liao, W.H. (2018). Anticorrosive, ultralight, and flexible carbon-wrapped metallic nanowire hybrid sponges for highly efficient electromagnetic interference shielding. Small *14*, 1–11. https://doi.org/10.1002/smll.201800534.

Yang, Y., Chen, S., Li, W., Li, P., Ma, J., Li, B., Zhao, X., Ju, Z., Chang, H., Xiao, L., et al. (2020a). Reduced graphene oxide conformally wrapped silver nanowire networks for flexible transparent heating and electromagnetic interference shielding. ACS Nano *14*, 8754–8765. https://doi.org/10.1021/acsnano.0c03337.

Yang, Y., Yamagami, Y., Yu, X., Pitchappa, P., Webber, J., Zhang, B., Fujita, M., Nagatsuma, T., and Singh, R. (2020b). Terahertz topological photonics for on-chip communication. Nat. Photonics *14*, 446–451. https://doi.org/10.1038/s41566-020-0618-9.

Yang, S., Wang, Y.Y., Song, Y.N., Jia, L.C., Zhong, G.J., Xu, L., Yan, D.X., Lei, J., and Li, Z.M. (2021). Ultrathin, flexible and sandwich-structured PHBV/silver nanowire films for high-efficiency electromagnetic interference shielding. J. Mater. Chem. C *9*, 3307–3315. https://doi.org/10.1039/d0tc05266c.

Zdrojek, M., Bomba, J., Lapińska, A., Dużyńska, A., Żerańska-Chudek, K., Suszek, J., Stobiński, L., Taube, A., Sypek, M., and Judek, J. (2018). Graphene-based plastic absorber for total sub-terahertz radiation shielding. Nanoscale *10*, 13426–13431. https://doi.org/10.1039/c8nr02793e.

Zhang, Z., Xiao, Y., Ma, Z., Xiao, M., Ding, Z., Lei, X., Karagiannidis, G.K., and Fan, P. (2019). 6G wireless networks: vision, requirements, architecture, and key technologies. IEEE Veh. Technol. Mag. *14*, 28–41. https://doi.org/10.1109/MVT.2019.2921208.

Zhou, B., Su, M., Yang, D., Han, G., Feng, Y., Wang, B., Ma, J., Ma, J., Liu, C., and Shen, C. (2020). Flexible MXene/silver nanowire-based transparent conductive film with electromagnetic interference shielding and electro-photo-thermal performance. ACS Appl. Mater. Inter. *12*, 40859–40869. https://doi.org/10.1021/acsami.0c09020.

STAR★METHODS

KEY RESOURCES TABLE

REAGENT or RESOURCE	SOURCE	IDENTIFIER
Chemicals, peptides, and recombinant proteins		
Acetone (99.8%)	Daejung Chemicals & Metals Co., Ltd	CAS: 67-64-1
Isopropyl alcohol (99.5%)	Daejung Chemicals & Metals Co., Ltd	CAS: 67-63-0
Silver nanowire	SG FLEXIO Co., ltd	http://www.flexiotech.com/ko/
Graphene oxide	GRAPHENEALL CO., LTD.	http://www.grapheneall.com/
Software and algorithms		
OriginPro 9.0	Origin Lab	https://www.originlab.com/
NI Labview 2018	National Instruments	https://www.ni.com/
Matlab R2018b	MathWorks	https://www.mathworks.com/
Comsol Multiphysics 5.3a	Comsol Multiphysics	https://www.comsol.com/
Other		
Mai Tai HP One Box Ti:Sapphire Ultrafast Lasers	Spectra-Physics	https://www.spectra-physics.com/f/mai-tai-ultrafast-laser
Auto Film Applicator	TESTER SANGYO Co., Ltd	https://www.tester.co.jp/products/pi/pi_1210-e.html

RESOURCE AVAILABILITY

Lead contact

Further information and requests for resources and reagents should be directed to and will be fulfilled by the lead contact, Minah Seo (mseo@kist.re.kr).

Materials availability

This study did not generate new unique reagents.

Data and code availability

- All data reported in this paper will be shared by the lead contact upon request.
- This paper does not report original code.
- Any additional information required to reanalyze the data reported in this paper is available from the lead contact upon request.

EXPERIMENTAL MODEL AND SUBJECT DETAILS

Our study does not use experimental models typical in the life sciences.

METHOD DETAILS

Sample preparation

Nanoslot arrays were patterned on a high-resistivity silicon substrate (>10,000 Ω cm, 675-μm thickness) using i-line stepper system (NSR-2005i10C; Nikon) to exclude attenuation by the substrate at a reliable THz regime and coated with a 150-nm-thick Au film, which is sufficiently thick to act as a perfect conductor (Lee et al., 2019). Each nanoslot was designed with a 500-nm width and 100-μm length to have a resonance frequency, f_{res}, of 0.65 THz. In addition, silver nanowires and graphene oxide (GO) were prepared to coat the nanoslot. Pristine silver nanowires (23-μm in length and 21-nm in diameter) were encapsulated by polyvinylpyrrolidone (PVP) and sprayed onto the nanoslot using an automatic film applicator (PI-1210; Sangyo, Japan). The PVP cladding layer is used to prevent oxidation of the silver nanowires but results in large contact resistance, which prevents charge transport between nanowires. Therefore, a sintering process was subsequently performed to eliminate the PVP layer and enhance the electrical network property of the

silver nanowires, as shown in Figure 1B. As presented in previous reports (Kim et al., 2018), the contact resistance of conductive films considerably decreases after chemical treatment and without a significant reduction in optical transparency. With such enhanced charge transport by decreasing the contact resistance, increased THz shielding can be expected. To further improve the electrical properties, GO (0.02 wt%) was sprayed and chemically reduced using a hydrazine agent to form a rGO film. Subsequently, the silver nanowire network was welded by the rGO, causing the film resistance to be reduced (Yang et al., 2020a). Additionally, the rGO/SSN film was coated on a polyethylene terephthalate (PET) substrate under the same process to prove the role of the nanoslot. Figure 1B shows a field-emission scanning electron microscopy (Nova SEM; FEI) image of the rGO/SSN coated on a PET substrate.

THz time-domain spectroscopy

THz transmittance was obtained using a THz-TDS system with a femtosecond Ti:sapphire laser (800-nm center wavelength and 80-MHz repetition rate with 100-fs pulse duration). The laser was divided in two directions by a beamsplitter for the THz emission and detection. THz pulses were generated from a photoconductive antenna driven by the fs laser beam, which was collimated and focused onto the sample using a polymethylpentene (TPX) lens pair. The transmitted THz waves were detected by an electro-optic sampling technique that measures the rotation angle of the polarization of the optical beam while traveling in a ZnTe crystal. THz signals were acquired from 0.2 to 2.0 THz with a high signal-to-noise ratio up to 70 dB. To obtain the THz transmission spectrum, measured time-domain THz waveforms were converted to frequency-domain data by the fast Fourier transform algorithm. THz transmittance of the sample ($T(\omega)$) is defined by $|E_{sample}(\omega)/E_{inc}(\omega)|^2$, where $E_{sample}(\omega)$ and $E_{inc}(\omega)$ are transmitted signals of the sample and silicon substrate (incident beam), respectively (Figure 2A).

QUANTIFICATION AND STATISTICAL ANALYSIS

Our study doesn't include quantification or statistical analysis.